

# Rapid Building Damage Estimates From the M7.8 Turkey Earthquake Sequence via Causality-Informed Bayesian Inference From Satellite Imagery

Earthquake Spectra

1–29

© The Author(s) 2024

Article reuse guidelines:

[sagepub.com/journals-permissions](https://sagepub.com/journals-permissions)

DOI: 10.1177/87552930241290501

[journals.sagepub.com/home/eqs](https://journals.sagepub.com/home/eqs)

Xuechun Li<sup>1</sup> , Xiao Yu<sup>2,3</sup>, Paula M. Bürgi<sup>3</sup>,  
David J. Wald<sup>4</sup> , Xie Hu<sup>2</sup>, and Susu Xu<sup>1</sup>

## Abstract

On February 6, 2023, a major earthquake of 7.8 magnitude and its aftershocks caused widespread destruction in Turkey and Syria, causing more than 55,000 deaths, displacing 3 million people in Turkey and 2.9 million in Syria, and destroying or damaging at least 230,000 buildings. Our research presents detailed city-scale maps of landslides, liquefaction, and building damage from this earthquake, utilizing a novel variational causal Bayesian network. This network integrates InSAR-derived change detection with new empirical ground failure models and building footprints, enabling us to (1) rapidly estimate large-scale building damage, landslides, and liquefaction from remote sensing data, (2) jointly attribute building damage to landslides, liquefaction, and shaking, (3) improve regional landslide and liquefaction predictions impacting infrastructure, and (4) simultaneously identify damage degrees in thousands of buildings. For city-scale, building-by-building damage assessments, we use building footprints and satellite imagery with a spatial resolution of approximately 30 meters. This allows us to achieve a high resolution in damage assessment, both in timeliness and scale, enabling damage classification at the individual building level within days of the earthquake. Our findings detail the extent of building damage, including collapses, in Hatay, Osmaniye, Adiyaman, Gaziantep, and Kahramanmaraş. We classified building damages into five categories: no damage, slight, moderate, partial collapse, and collapse. We evaluated damage estimates against preliminary ground-truth data reported by the civil authorities.

<sup>1</sup>Department of Civil and System Engineering, Johns Hopkins University, Baltimore, MD

<sup>2</sup>College of Urban and Environmental Sciences, Peking University, Beijing, China

<sup>3</sup>Department of Earth and Atmospheric Sciences, University of Houston, TX

<sup>4</sup>U.S. Geological Survey, Golden, CO

## Corresponding author:

Susu Xu, Department of Civil and System Engineering, Johns Hopkins University, 3400 N Charles St, Latrobe Hall 201, Baltimore, MD 21218, USA.

Email: [susuxu@jhu.edu](mailto:susuxu@jhu.edu)

Our results demonstrate the accuracy of our classification system, as evidenced by the area under the curve (AUC) scores on the receiver operating characteristic (ROC) curve, which ranged from 0.9588 to 0.9931 across different damage categories and regions. Specifically, our model achieved an AUC of 0.9931 for collapsed buildings in the Hatay/Osmaniye area, indicating a 99.31% probability that the model will rank a randomly chosen collapsed building higher than a randomly chosen non-collapsed building. These accurate, building-specific damage estimates, with greater than 95% classification accuracy across all categories, are crucial for disaster response and can aid agencies in effectively allocating resources and coordinating efforts during disaster recovery.

### Keywords

causal Bayesian network, joint hazards estimation, post-earthquake response, building damage class identification, satellite imagery

Date received: 4 December 2023; accepted: 18 August 2024

## Introduction

Information about building damage caused by earthquakes is critical for effective disaster response and recovery mitigation efforts, given their significant impact on infrastructure and human lives. Up to now, mapping out individual building damage in a large-scale seismic zone has been beyond the capacity of rapid, regional loss models (e.g., USGS PAGER system (Earle et al. 2009)), nor has satellite imagery been sufficiently exploited to rapidly recognize and quantify such detailed impacts. Additionally, earthquake shaking often induces ground failure, such as landslides and solid liquefaction, that can happen concurrently and collocate with damage caused by shaking (Bird et al. 2006; Fan et al. 2019). These ground failures may further induce or exacerbate building damage. In this study, we focus on the Mw 7.8 earthquake and its aftershocks that struck southern Turkey and Syria in February 2023, causing extensive building damage and large-scale landslides and liquefaction.

As of February 14, 2023, NASA's Goddard Space Flight Center, utilizing satellite imagery, identified more than 100 landslides in the areas of Turkey affected by the M7.8 mainshock on February 6, 2023, and the M7.5 aftershock later that same day (SciTechDaily 2023). Additionally, thousands more landslides have been reported by early field reconnaissance teams, indicating a more extensive ground-level impact than initially observed from satellite data (Seismological Society of America 2023). Post-disaster reporting also identified 760 sites with liquefaction and lateral spreading features (Maria et al. 2023; Cetin et al. 2024; Ozkula et al. 2023). Both landslides and liquefaction exacerbate damage to buildings and infrastructure, compounding the vast shaking-induced losses. Preliminary investigations show that in all, this earthquake sequence destroyed or damaged more than 230,000 buildings, causing the vast majority of nearly 55 thousand lives lost, and hundreds of thousands of injuries (U.S. Geological Survey 2023b,a). Immediate information on the location and severity of disaster-induced ground failure and building damages is essential for accurately understanding seismic impacts (Xu et al. 2022b; Wang et al. 2023a). Yet, the vast scale of such a disaster—over 110,000 square kilometers and potentially millions of buildings affected—dwarfs current strategies for quantifying such losses in any detail. After the 2023 Turkey–Syria earthquake sequence, which is primarily characterized by the M7.8 mainshock on February 6, 2023, followed by the significant M7.5 aftershock later on



**Figure 1.** Damage proxy maps (DPM) generated by the AIRA team (ARIA Data Share 2023a) after the M7.8 Turkey–Syria earthquake, covering the area between  $36^{\circ}62'E$  to  $37^{\circ}87'E$  longitude and  $36^{\circ}64'N$  to  $37^{\circ}66'N$  latitude. The grayscale gradient indicates the level of detected damage, where a value of 0 represents no damage and a value of 1 indicates maximum damage. A scale bar in the lower left corresponds to 20 km, aiding in the estimation of affected areas' extents.

the same day, various methods were proposed to estimate building damage (CrisisReady 2023). Furthermore, existing regional loss models focus only on simulating the direct effects of ground shaking on building damage without accounting for the additional consequences of associated landslide and liquefaction hazards.

Remote sensing techniques, such as synthetic aperture radar (SAR) images, have been widely utilized, primarily qualitatively, to provide high-resolution information for rapid hazard and impact evaluations (Loos et al. 2020; Yun et al. 2015; Barras 2007; Li et al. 2023b; Xu et al. 2022b; Wang et al. 2023b; Yu et al. 2024; Wald et al. 2022b; Xu et al. 2022c). Interferometric SAR (InSAR) images, available within hours to days after an event, have the potential to provide high-resolution information about post-disaster ground failure or building damage, taken in all weather conditions and at any time of the day or night (as opposed to optical satellite images), which are only useful when acquired during the day and in cloud-free conditions (Lee 2005; Zhao and Lu 2018). After the Mw 7.8 earthquake sequence in southern Turkey, the Advanced Rapid Imaging and Analysis (ARIA) team generated a damage proxy map (DPM), shown in Figure 1, depicting earthquake-induced surficial changes that alter radar reflectivity. The DPM was generated using data from descending track P21 using coherence between pre-earthquake SAR images taken from September 19, 2022, to January 29, 2023, and post-earthquake SAR images taken on February 10, 2023, by the Sentinel-1 satellites operated by the European Space Agency (ARIA Data Share 2023b). A known limitation of DPM alone is that significant radar differences depict complex sources of changes—including building damage, ground changes, and noise (snow cover, vegetation, anthropogenic changes) and cannot

differentiate among these causes—limiting their utility and providing little guidance to decision-makers.

Instead, using causal modeling techniques, our approach integrates single-type hazard geospatial models with rich but noisy information from DPM to estimate building and infrastructure damage jointly induced by ground shaking and ground failure. Our method encodes existing USGS ground failure products (Zhu et al. 2015; Nowicki Jessee et al. 2018), which provide probability estimates of landslides and liquefaction in this earthquake, composite ground shaking of earthquake sequence, building damage, remote sensing observations, and environmental noise in a causal graph and links them with causal physical dependencies. In earlier work, we were able to show—by hindcasting with data from previous earthquakes—the utility of our new variational inference, causal Bayesian network model to not only separate and map out different earthquake-induced hazards (shaking, landslides, and soil liquefaction) but also to then identify damage to buildings and attribute their cause to each of these hazards in a probabilistic sense via the causal graph (Xu et al. 2022b; Li et al. 2023a; Xu et al. 2022a).

After being notified about initial loss estimates due to this earthquake, we immediately set out to apply those new tools to the preliminary models and available datasets needed in our application, namely the USGS ShakeMap, landslide and liquefaction estimates, and the DPM imagery, and obtain building damage estimates as well as updated landslides and liquefaction estimates within two hours. Specifically, because we are able to leverage recently improved building footprints (Microsoft 2023) and high-resolution (but noisy) satellite imagery, we can achieve unprecedented damage resolution with unparalleled timeliness and scale, enabling response and aid agencies to make well-informed decisions on resource allocation and coordination of recovery efforts in the aftermath of this and potentially other similar disasters. With this approach, we provide our first-version large-scale building damage estimates for the most moderately damaged areas, covering several major cities in the seismic zone, including Hatay, Osmaniye, Gaziantep, Kahramanmaraş, and Adıyaman, a preliminary version of which was provided to via a rapid report delivered to the DesignSafe web portal on March 1, 2023 (Li et al. 2023b), aimed at informing ongoing and future reconnaissance teams. Though we have not yet achieved a fully operational system, here we show the potential for this strategy to provide rapid and detailed building damage assessments in the immediate aftermath of any such disaster in the future. Full validation of the results presented here awaits detailed ground-truth observations currently being collected and analyzed by numerous reconnaissance field teams and being poured over by careful, manual analyses of optical and radar imagery. We expect that comprehensive landslide and liquefaction datasets being slowly and meticulously compiled at this time will yield ground truth data that will allow us to not only fully quantify the accuracy of our building damage estimates but also allow for a comprehensive comparison of our model's landslide and liquefaction estimates in areas without buildings.

## Data and Methods

Our variational causal Bayesian inference framework allows us to jointly estimate ground failure and building damage. We formulated a causal Bayesian network based on the potential causal relationships among prior geospatial models, building footprints, DPM, unobserved ground failure, and unobserved building damage, underlying the geological processes. We present our Bayesian network in Figure 3. The framework outputs

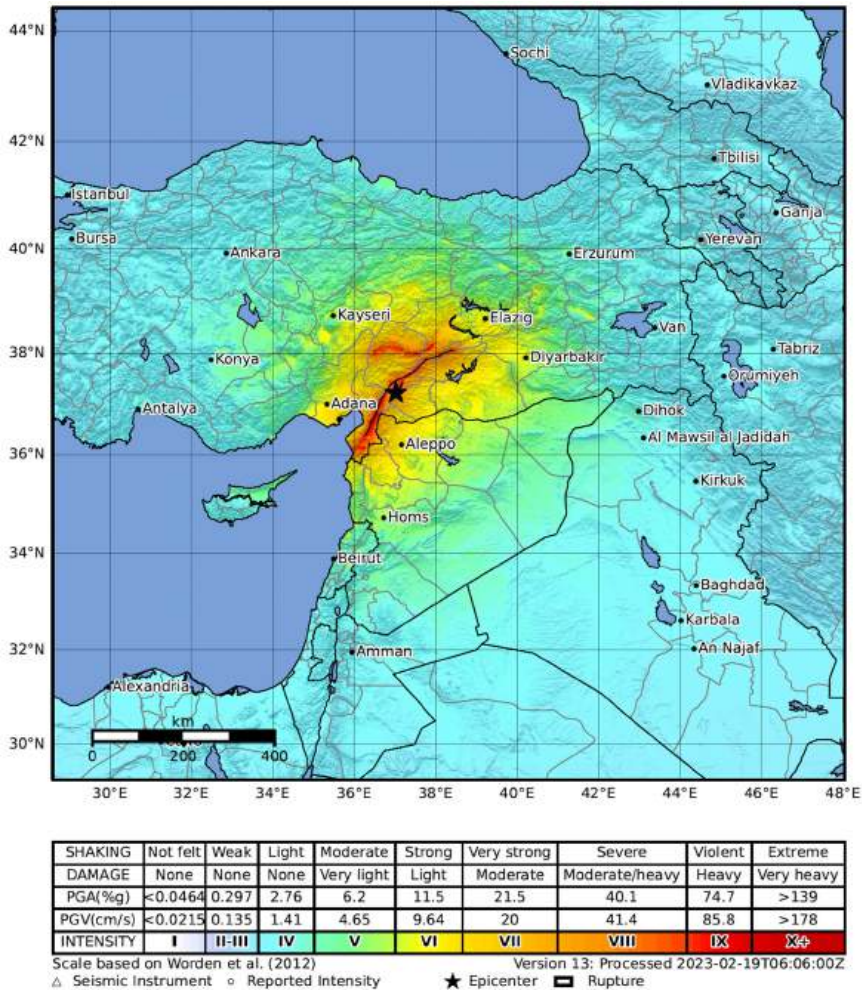


**Figure 2.** Composite ShakeMap, developed by the USGS ShakeMap team, depicting the strongest shaking due to any of magnitude 5.5 and larger events of the sequence (U.S. Geological Survey 2023d) the 2023 Turkey–Syria earthquake sequence, as of Feb. 19, 2023. The shaking intensity scale is based on (Worden et al. 2012).

probability maps for ground failure, building damage, and parameters representing their causal dependencies.

### Prior Geospatial Models

The basic driver of building damage and the triggering of landslides and liquefaction is the extent of and intensity of shaking, which we import directly from USGS ShakeMap (U.S. Geological Survey 2023e). Given the large shaking footprint of both the large Mw 7.8 and subsequent Mw 7.5 event as well as from 15 other Mw 5.5 aftershocks, USGS generated a composite ShakeMap (U.S. Geological Survey 2023e) depicting the strongest shaking estimate at every location from all of the events, which is shown in Figure 2. Because the

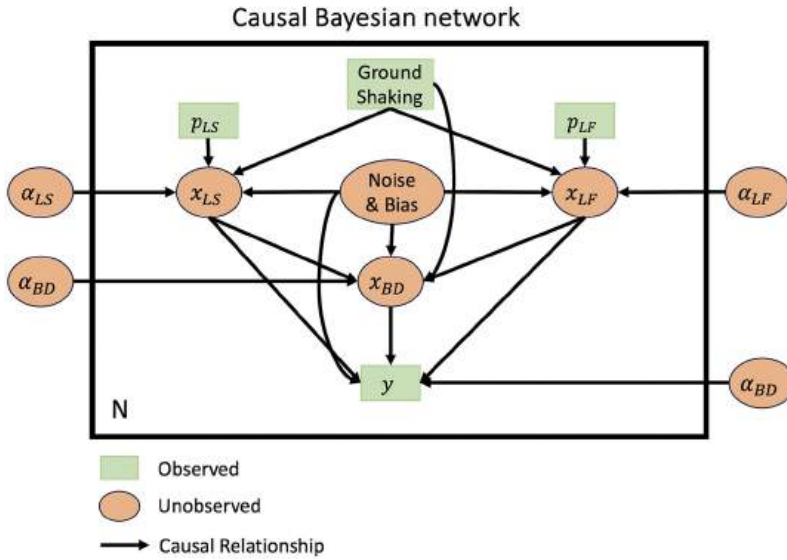


**Figure 3.** Causal Bayesian network that depicts the causal relationships among ground failure models,  $p_{LS}$  and  $p_{LF}$ , latent hazards and impact, sensing observation ( $y$ ).  $N$  refers to  $N$  locations in a target area. Green rectangles refer to the known variables. Blue circles refer to unobserved or unknown nodes.  $\alpha_i$  are the unknown causal parameters that quantify the causal relations among parent nodes and child nodes.

composite ShakeMap more effectively represents the maximum shaking experienced than any individual event, it can be used for better estimates of damage, landslides, and liquefaction and is quite useful for earthquake engineering forensics, more generally (Wald et al. 2022a).

In addition to ShakeMap, as part of the suite of their rapid, post-earthquake information products (Wald et al. 2003), USGS added rapid ground-failure estimates—models of the extent and probability of earthquake-shaking triggered landslides and liquefaction in 2018 (Allstadt et al. 2022). In addition to shaking, the models employ slope, susceptibility, and soil conditions to map these probabilities (Zhu et al. 2015; Nowicki Jessee et al. 2018), as shown in Figure 4. We use the existing USGS ground failure products as our prior landslide and liquefaction models in our Bayesian network, which are nodes  $p_{LS}$  and  $p_{LF}$  in Figure 3.

### *InSAR Data and Damage Proxy Maps*

Following the Turkey–Syria earthquake sequence, the ARIA team ([ARIA Data Share 2023a](#)) generated a DPM utilizing SAR images taken by the Sentinel-1A satellite operated by the European Space Agency (ESA). The DPM we employ is shown in Figure 1. We utilize DPM as our sensing observations because—despite being noisy—they provide high-resolution (typically 30-meter pixels or finer) pre- and post-earthquake surfacial changes related to earthquake-induced ground failure and building damage. The coverage of the DPM is from 36.623 °E to 37.969 °E, from 36.641 °N to 37.662 °N, which covers the cities analyzed in this paper: Kahramanmaraş, Osmaniye, Gaziantep, Adıyaman, and Hatay.

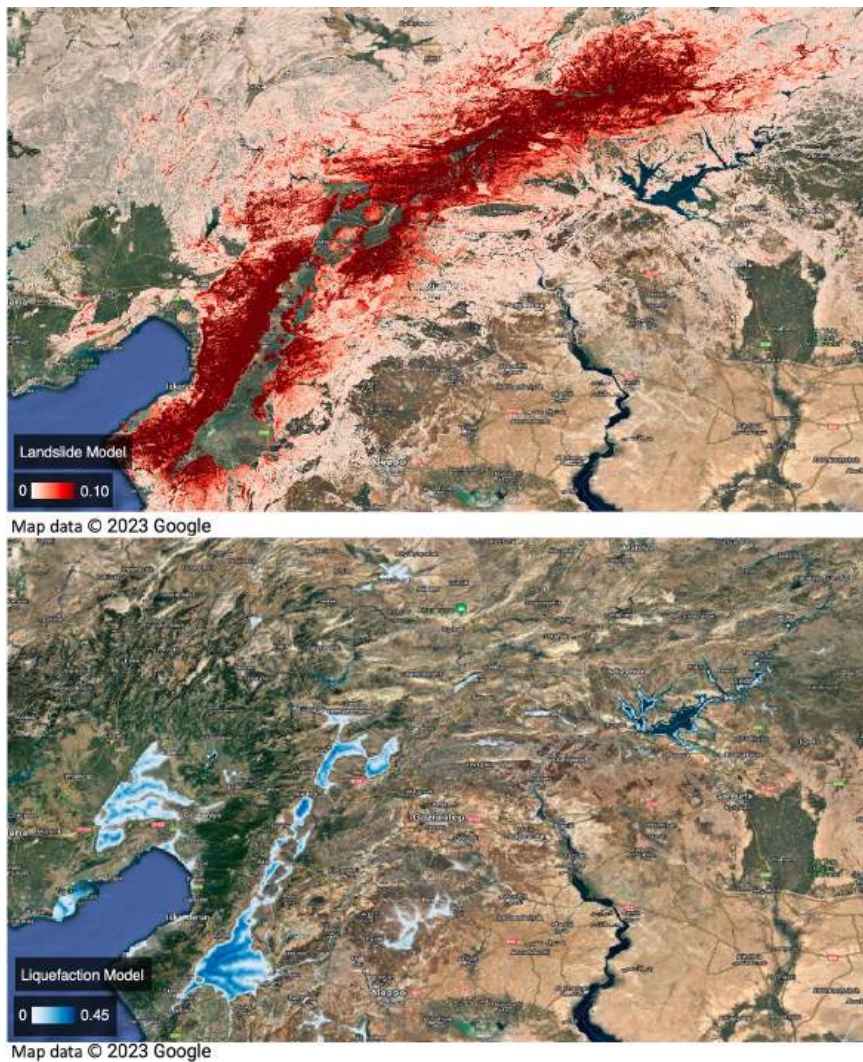


**Figure 4.** Example of ground failure models for landslide and liquefaction produced by the USGS (U.S. Geological Survey 2023c) after the 2023 Turkey–Syria earthquake sequence. The legend colors represent the probability of ground failure models.

We do not include cities located in regions where the DPM signal may be heavily impacted by known noise sources, such as snow cover and high tectonic strain.

### *The Joint Ground Failure and Building Damage Estimation Method*

Key obstacles to accurately estimating building damage after an earthquake include the co-location of disaster-induced multiple subsequent ground failure and building damage, as well as distribution shifting across different buildings Xu and Noh (2021). Additionally, we necessarily employ relatively coarse, regional-scale, shaking, damage, and ground failure models. In fact, obtaining more detailed damage models is beyond the current state of the art, owing to the lack of detailed building inventories (beyond footprints—structural

details are needed for each) and the uncertainties introduced not only by coarse shaking estimates but also in the uncertain relationships between shaking and damage (fragility curves) (Jaiswal et al. 2010). For ground failure estimates, in addition to shaking uncertainties, relatively coarse slope values and approximate proxies for susceptibility limit accuracy (Allstadt et al. 2022).

To address the limitations in joint estimation of building damage and ground failure, we previously introduced a variational causal Bayesian inference framework (Xu et al. 2022b). Our approach leverages causal Bayesian networks to model the complex relationships between building damage, ground failure, and other relevant factors. By encoding prior knowledge and physical constraints into the network structure, we can capture the causal dependencies among these variables.

Our model uniquely integrates coarser-scaled, physics-based prior models of shaking and ground failure with detailed building footprints and the high-resolution, yet less informed, changes detected in pre- and post-event DPM. The inference process involves estimating the probability maps of unobserved variables and learning the causal coefficients through a variational algorithm. This allows us to discern the causes of detected changes in the DPM by providing context from the prior models. For instance, damage in low-slope regions is unlikely due to landslides, while damage in high-slope areas is not attributed to liquefaction. Similarly, damage in urban regions with low probability of ground failure is likely due to shaking.

The integration of multiple sources of information and joint modeling of building damage and ground failure enables our framework to achieve a level of inference and specificity in damage causation that is not possible with models assessing a single hazard or those not updating their estimates based on the latest high-resolution imagery. By quantifying the uncertainties associated with the predictions, our approach provides more accurate and interpretable results for disaster management and risk assessment.

In this work, we model the causal Bayesian network, which is shown in Figure 3, to represent the causal dependencies among building damage (BD), landslides (LS), liquefaction (LF), and DPM. All datasets in this work are maps with size  $l = 1, \dots, N$ . We define  $y^l$  as our observed variable (DPM) and  $x_h^l$  as the unobserved hazard nodes, where  $h \in LS, LF, BD$ . We assume these nodes are binary with values zero and one, where zero represents no hazard happens and one represents hazard happens. We define a bias node  $x_0$  that is always active ( $x_0 = 1$ ). This bias node allows its child nodes to be active even when other parent nodes are inactive.  $\mathcal{P}(i)$  represents parent nodes of a node  $i$ . All nodes are linked by an arbitrary directed acyclic graph. We assume the underlying causal dependencies from parent nodes to unobserved  $x_h^l$  as:

$$\log \frac{p(x_h=1|\mathcal{P}(x_h), \epsilon_h)}{1-p(x_h=1|\mathcal{P}(x_h), \epsilon_h)} = w_{0h} + w_{\epsilon_h} \epsilon_h + \sum_{k \in \mathcal{P}(x_h)} w_{kh} x_k \quad (1)$$

The formulation of underlying causal dependencies from parent nodes to DPM ( $y$ ) is assumed as:

$$\log y = w_{\epsilon_y} \epsilon_y + w_{0y} + \sum_{i \in \mathcal{P}(y)} w_{iy} x_i \quad (2)$$



where  $\epsilon$  is normally distributed.

We then employ a variational Bayesian inference method to estimate the posterior distributions of unobserved ground failure and building damage by maximizing the log-likelihood of observed variables. To guarantee our method's scalability, variational inference is carried out iteratively on a small batch of locations, which are randomly selected in each iteration. For every location  $l$ , a variational distribution  $q(X^l)$  is defined, which is further decomposed across unobserved nodes as:

$$q(X^l) = \prod_i q(x_i^l) = \prod_i (q_i^l)^{x_i^l} (1 - q_i^l)^{1-x_i^l} \quad (3)$$

Given a map with a set of locations  $N$ , we proceed to derive a tight lower bound for the log-likelihood as Xu et al. (2022b):

$$\begin{aligned} \mathcal{L}_v \geq & \sum_l \left\{ -\log y^l - \log w_{\epsilon_y} - \frac{(y^l)^2 + w_{0y}^2}{2w_{\epsilon_y}^2} \right. \\ & - \frac{\sum_{k \in \mathcal{P}(y^l)} w_{ky}^2 q_k^l + 2w_{0y} \sum_{k \in \mathcal{P}(y^l)} w_{ky} q_k^l}{2w_{\epsilon_y}^2} \\ & + \frac{2w_{0y} \log y^l - 2\log y^l (\sum_k w_{ky} q_k^l)}{2w_{\epsilon_y}^2} \\ & - \frac{\sum_{k,l} 2w_{ky} w_{ly} q_k^l q_l^l}{2w_{\epsilon_y}^2} - \sum_h [q_h^l \log q_h^l \\ & + (1 - q_h^l) \log(1 - q_h^l)] - \sum_{h \in \{LS, LF\}, m \in \{0, 1\}} (q_h^l)^m \times \\ & (1 - q_h^l)^{1-m} \log \left( 1 + \exp \left( (-1)^m (w_{0h} + w_{\alpha_h} \alpha_h) + \frac{w_{\epsilon_h}^2}{2} \right) \right) \\ & - \sum_{m, n \in \{0, 1\}, k \in \mathcal{P}(BD)} \left( 1 + \exp \left[ (-1)^m \left( w_{0BD} \right. \right. \right. \\ & \left. \left. \left. + \sum_{k \in \mathcal{P}(BD)} \frac{1 - (-1)^n}{2} w_{kBD} \right) + \frac{w_{\epsilon_{BD}}}{2} \right] \right) \\ & \left. \prod_{k \in \{BD, \mathcal{P}(BD)\}} (q_k^l)^{m_k} (1 - q_k^l)^{1-m_k} \right\} \end{aligned}$$

Our ultimate goal is to optimize the bound in order to identify the best combinations of posterior probabilities and causal dependency estimates. Since both the posteriors and weights are unknown, we employ an expectation-maximization approach to tackle this problem. During the expectation step, we obtain closed-form update equations for the local posterior probabilities of LS, LF, and BD (denoted as  $q_h^l$ , where  $h \in LS, LF, BD$  and  $l \in N$ ) by maximizing the lower bound and setting its gradients to zero. We compute this gradient using the chain rule, and the optimal posterior follows the form described below:

$$q_i^l = \frac{1}{1 + \exp(-\mathcal{T}(q_{\mathcal{P}(i)}, q_{S(i, C(i))}, q_{C(i)}, y^l, w))} \quad (4)$$

where  $\mathcal{P}(i)$  represents the set of parent nodes for node  $i$ , while  $\mathcal{C}(i)$  denotes the set of child nodes for node  $i$ .  $\mathcal{S}(i)$  refers to the set of spouse nodes that have common child nodes with node  $i$ . Function  $\mathcal{T}$  is determined by the following form:

$$\begin{aligned}
 T(i) = & \sum_{k \in \mathcal{P}(i), v \in \{0, 1\}} \left\{ (-1)^v q_k f \left( (-1)^v (w_{0i} + w_{ki}) + \frac{w_{ei}^2}{2} \right) \right. \\
 & \left. + (-1)^v (1 - q_k) f \left( (-1)^v w_{0i} + \frac{w_{ei}^2}{2} \right) \right\} \\
 & \sum_{k \in \mathcal{C}(i), k \neq y, v \in \{0, 1\}} \left\{ (-1)^v q_k f \left( (-1)^v (w_{0i} + w_{ik}) \right. \right. \\
 & \left. \left. + \frac{w_{ek}^2}{2} \right) + (-1)^v (1 - q_k) f \left( (-1)^v w_{0i} + \frac{w_{ek}^2}{2} \right) \right\} \\
 & - \frac{2 \sum_{m \in \mathcal{S}(i), y} w_{iy} w_{my} q_m}{2w_{ey}^2} \\
 & + \frac{(2y - 2w_{0y} - w_{ey}^2) w_{iy}}{2w_{ey}^2}
 \end{aligned} \tag{5}$$

where  $f(x) = \log(1 + \exp(x))$  to ensure that the posterior has the value between 0 and 1.

During the maximization step, we perform updates using stochastic gradient descent to estimate the optimal weights. These updates utilize a mini-batch of data, which is randomly selected from various locations. We employ stochastic variational inference to speed up the computational process across a large, high-resolution map. Consequently, the edge weights at iteration  $t + 1$  are updated as follows:

$$\mathbf{w}^{(t+1)} = \mathbf{w}^{(t)} + \rho \cdot A \nabla L^{(t)}(\mathbf{w})$$

We also employ a local pruning algorithm to speed up computations across a large area. This approach is inspired by the realization that causal graphs in real-world scenarios are generally sparse, meaning only a limited number of nodes remain active. For instance, areas lacking building footprints will not experience building damage, making the building damage nodes inactive. Consequently, we can eliminate these inactive nodes and retain only those that are active and essential for updating parameters. For each location, we first apply local pruning to generate a local model, and then implement stochastic variational inference on this model. Our theoretically derived variational bound is applicable to any network that shares a similar structure and variable assumptions as ours. This allows for easy adaptation of the stochastic variational inference algorithm by setting the posterior  $q_h$  of inactive nodes  $h$  to zero. By combining stochastic variational inference with local pruning, we significantly lower both computational expenses and memory requirements.

## Results

We visualize the results of our predicted building damage probability maps along with comparisons with post-earthquake satellite images provided by Google Maps. The images were captured after the earthquake that occurred on February 16, 2023. To enhance the interpretation of building damage probability maps, we categorize the building damage probability into four levels: slight damage (including no damage) (probability  $\leq 0.3$ ),

**Table 1.** Building damaged levels classification of ground truth information.

Original damage state in Turkish	Original damage state in English	Reclassified damage state in English
Az Hasarlı	Slightly Damaged	Slightly Damaged
Ağır Hasarlı	Heavily Damaged	Moderately/Severely Collapsed
Acil Yıkılacak	Needs to be Demolished	Partially Collapsed
Yıkık	Collapsed	Collapsed

moderate damage ( $0.3 < \text{probability} \leq 0.65$ ), partial collapse ( $0.65 < \text{probability} \leq 0.8$ ), and collapse ( $\text{probability} > 0.8$ ). We adjust the threshold to align optimally with the limited available ground truth information; however, we expect that with a complete inventory, we can later constrain these ranges quantitatively. The damage levels we used are consistent with the EMS-98 intensity scale (Grünthal 1998).

We downloaded the ground truth information from the 2023 Turkey Earthquakes Building Damage Assessment Map (hereafter referred to as “Damage Assessment Map”), which classified four building damage levels: slightly damaged (az Hasarlı), heavily damaged (ağır Hasarlı), needs to be demolished (acil Yıkılacak), and collapsed (yıkık). The damaged state “needs to be demolished” is the same as “partially collapsed” in the EMS-98 scale. They classified their damaged states according to the report by the Turkish Ministry of Environment (Dilsiz et al. 2023). However, the damage state terminologies used in Damage Assessment Map do not match with the terminologies in (Dilsiz et al. 2023; Grünthal 1998). Thus, we compared the data distribution from Damage Assessment Map with the data from the Turkish Ministry of Environment (Dilsiz et al. 2023) and re-assigned the damaged levels to the ground truth data we downloaded from Damage Assessment Map. We find out the ratios of slightly damaged, need to be demolished/partially collapsed, and collapsed in the ground truth data from Damage Assessment Map match the ratios of corresponding damaged states in Dilsiz et al., 2023. The ratio of heavily damaged in Damage Assessment Map does not match the ratio of either moderately damaged or severely damaged in (Dilsiz et al. 2023). However, it matches the combination of moderately and severely damaged in (Dilsiz et al. 2023). Thus, we reclassified heavily damaged in Damage Assessment Map to be moderately/severely damaged. The final classification of damage states of our ground truth information is shown in Table 1. In this analysis, we do not mark or label buildings inferred to be undamaged.

Figure 5 displays three zoomed-in locations in Kahramanmaraş, with Figure 5(a)–(c) presenting the satellite images and Figure 5(d)–(f) showing the corresponding building damage estimates (colored outlines) with ground truth damage observations (colored dots). Our models assign higher probabilities to collapsed or moderately damaged buildings, consistent with the ground truth images. On the other hand, buildings not damaged in the ground truth images, such as those in Figure 5(c), are assigned lower probabilities in our estimates, which we classify to be slightly damaged. Our probability-based damage maps accurately predict moderately damaged or collapsed buildings in the area shown in Figure 5(e), as validated by the corresponding ground truth information and satellite images in Figure 5(b). Separating undamaged and slightly damaged structures has been a fundamental challenge with imagery alone (Bai et al. 2020), yet we have the advantage here of employing shaking as a correlative, and we are working on improving prior building damage models, which will, hopefully, better inform even lower damage grades.

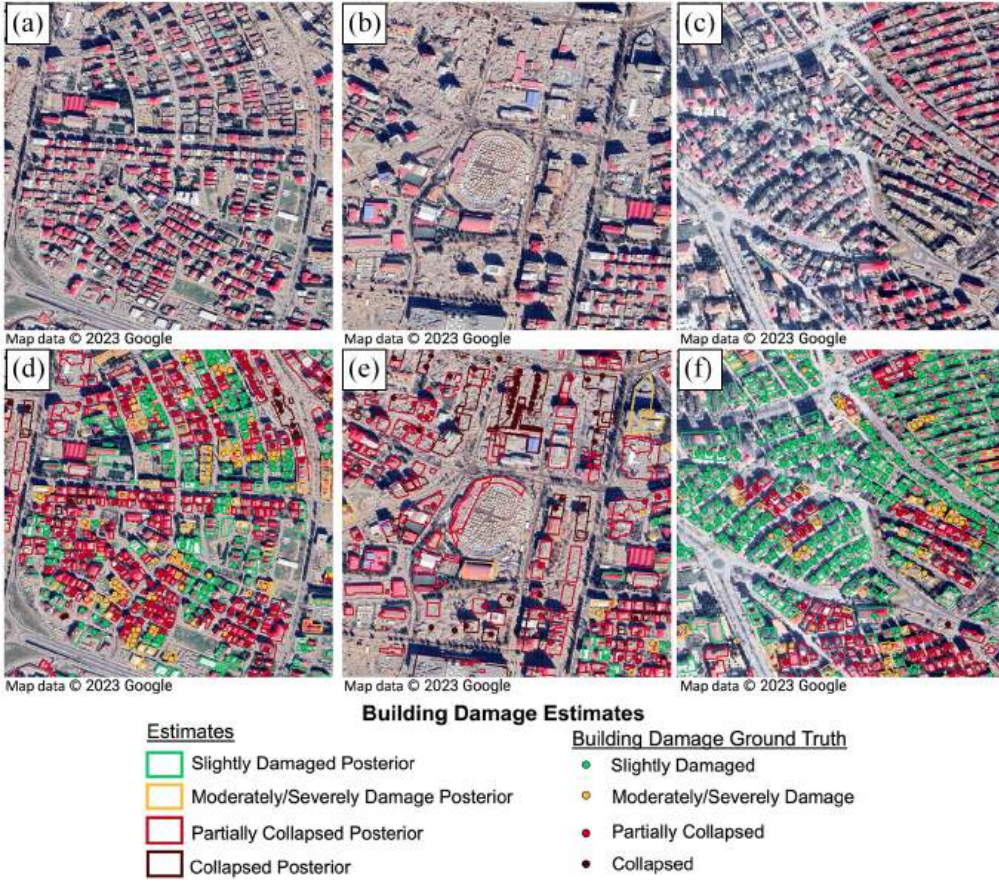


**Figure 5. Predicted building damage probability maps in Kahramanmaraş.** Figures (a)–(c) show the satellite images, and Figures (d)–(f) present the corresponding building damage estimates with ground truth information. The legend colors represent the building damage levels, as indicated. The geographic extent of each figure is given in Table 4 and Figure 13(1).

Figure 6 visualizes our probability-based building damage estimations in three locations with dense building distribution in Osmaniye. Our models accurately assign low probabilities to buildings that are not moderately damaged, as validated by the corresponding satellite images in Figure 6(b)(c) and also by the ground truth information presented in Figure 6(e)(f). Conversely, buildings that are collapsed or moderately damaged, as shown in Figure 6(a), are assigned high probabilities in our estimation, as demonstrated in Figure 6(d).

In Gaziantep, Figure 7 presents our building damage probability-based estimates in three locations. The corresponding satellite images in Figure 7(a)–(c) demonstrate that most buildings in these areas were not damaged or slightly damaged, which are assigned low probabilities by our models in Figure 7(d)–(f). Finally, Figure 8 shows our building damage estimates in three zoom-in locations in Adıyaman, where most buildings in the areas of (f) are predicted to be partially collapsed or collapsed. According to a post-earthquake report, extensive liquefaction was observed at the shores of lakes in Gölbaşı (Adıyaman), in the İskenderun Port wharf area, and in Antakya near the Asi River

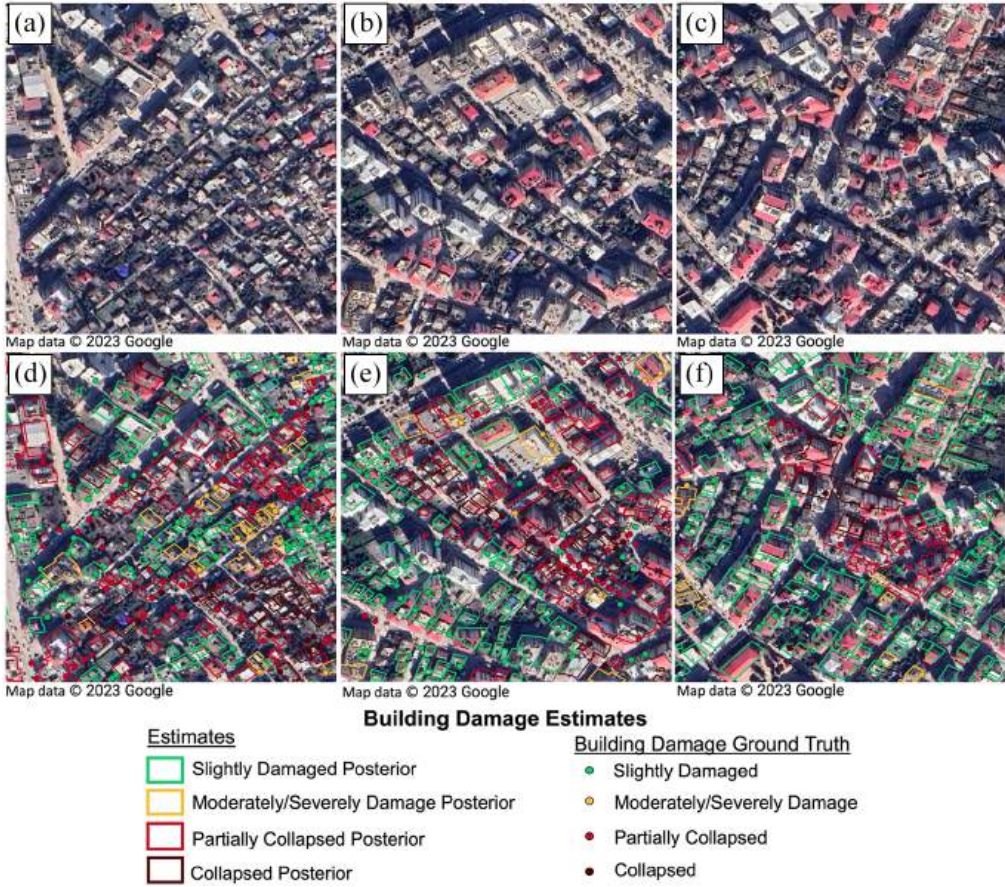


**Figure 6. Predicted building damage probability maps in Osmaniye.** Figures (a)–(c) show the satellite images, and Figures (d)–(f) present the corresponding building damage estimates with ground truth information. The legend colors represent the building damage levels, as indicated. The geographic extent of each figure is given in Table 4 and Figure 13(2).

(PreventionWeb 2023). This suggests that the Adiyaman may have also experienced severe liquefaction, which could have contributed to the moderate building damage and collapse observed in our estimates.

Figure 9 shows three zoomed-in areas in the city of In Hatay with post-earthquake satellite images, our probability-based building damage estimates, and the ground truth observations. Most buildings in these areas are moderately damaged or collapsed, which our models assign high probabilities and classify them to be partially collapsed or collapsed. Figure 10 depicts three zoom-in areas in İskenderun, Hatay, along with the corresponding satellite images and our building damage probability maps. Our estimates demonstrate that a large number of buildings in İskenderun are slightly damaged, while some of them collapsed. Our results are consistent with the slight damage and collapse observed in the satellite images taken on February 16 in Figure 10(a)–(c) and the ground truth assignments presented in Figure 10(d)–(f). According to post-earthquake reports, liquefaction manifestations were found from Antakya coastal plain up to Golbasi Lake to

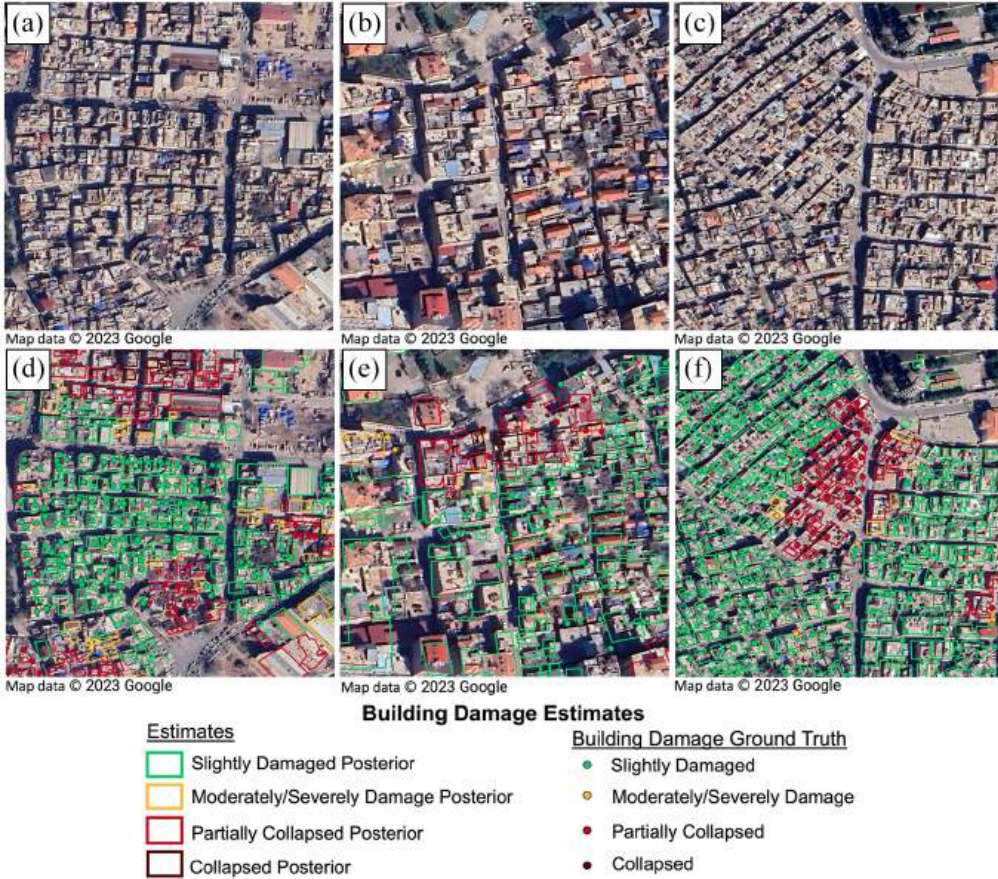


**Figure 7. Predicted building damage probability maps in Gaziantep.** Figures (a)–(c) show the satellite images, and Figures (d)–(f) present the corresponding building damage estimates with ground truth information. The legend colors represent the building damage levels, as indicated. The geographic extent of each figure is given in Table 4 and Figure 14(1).

the northeast, suggesting that this region may have been particularly susceptible to the effects of liquefaction (Maria et al. 2023). Thus, earthquake-induced liquefaction may have contributed to the moderate damage and collapse observed in many buildings in Adiyaman. Integrating our building damage estimates with observations from post-earthquake reports enhances our understanding of the damage causes in the region. Furthermore, a detailed analysis that correlates these estimates with field reports of liquefaction can shed light on the underlying reasons for the moderate damage and collapses that were observed in Adiyaman. This approach enables a more nuanced interpretation of the factors contributing to the observed patterns of destruction.

We can evaluate our estimates with the preliminary building damage investigation results from the Türkiye Ministry of Environment, Urbanization, and Climate Change from Damage Assessment Map. The Ministry classified building damage into four categories: slightly damaged, heavily damaged, needs to be demolished, and collapsed. We obtained a total of 198,633 data points corresponding to the four categories of building

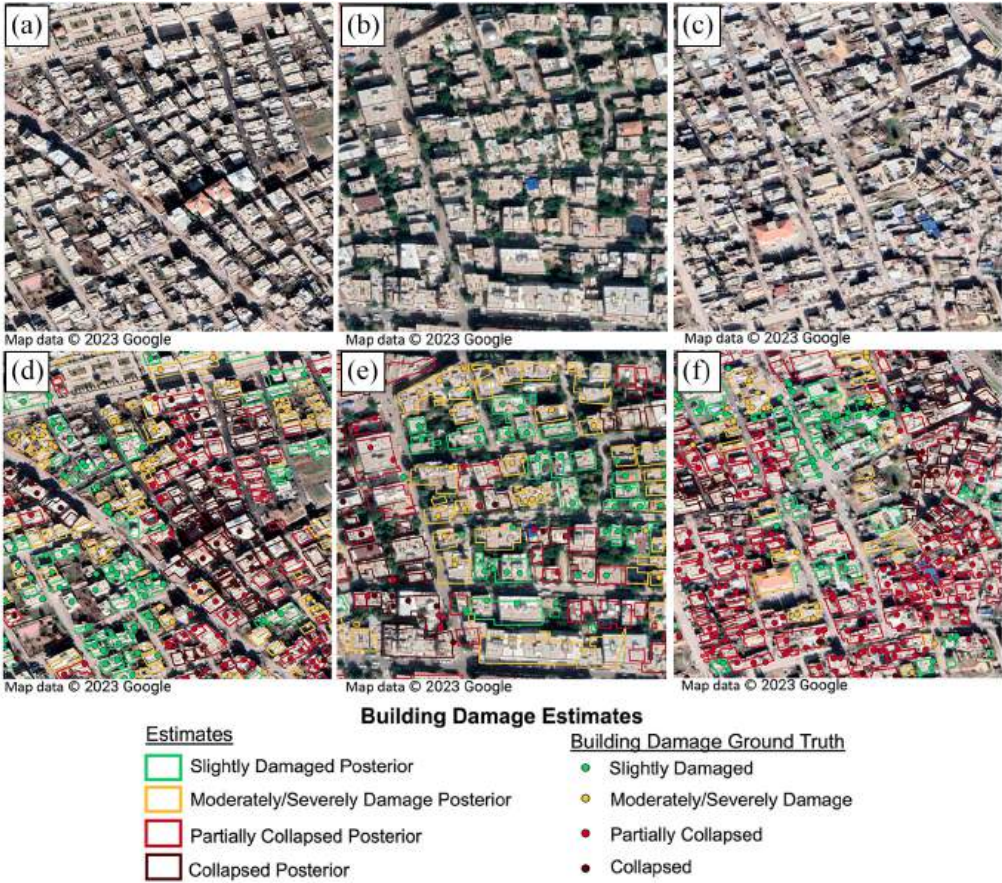


**Figure 8. Predicted building damage probability maps in Adiyaman.** Figures (a)–(c) show the satellite images, and Figures (d)–(f) present the corresponding building damage estimates with ground truth information. The legend colors represent the building damage levels, as indicated. The geographic extent of each figure is given in Table 4 and Figure 14(2).

damage from Damage Assessment Map, which show that there are 140,200 slightly damaged buildings, 42,482 heavily damaged buildings, 5714 partially collapsed (need to be demolished) buildings, and 10,237 collapsed buildings in the affected region. The reported percentages of each building damage level in our studied regions are given in Table 2. We further compare our probability maps from Damage Assessment Map with the preliminary official investigation results. The onsite building damage investigation and assessment activities are still ongoing as of mid-April 2023, so the reported damage numbers are far from complete.

We evaluated our estimates by plotting the receiver operating characteristics (ROC) curve and calculating the area under the ROC curve (AUC) values. The ROC curve shows the relationship between the true positive rate (TPR) and the false positive rate (FPR) of a binary classifier system, with TPR representing the probability of correctly predicting damage given that damage has occurred and FPR being the probability of incorrectly predicting damage given that no damage has occurred. A model with an AUC near 1

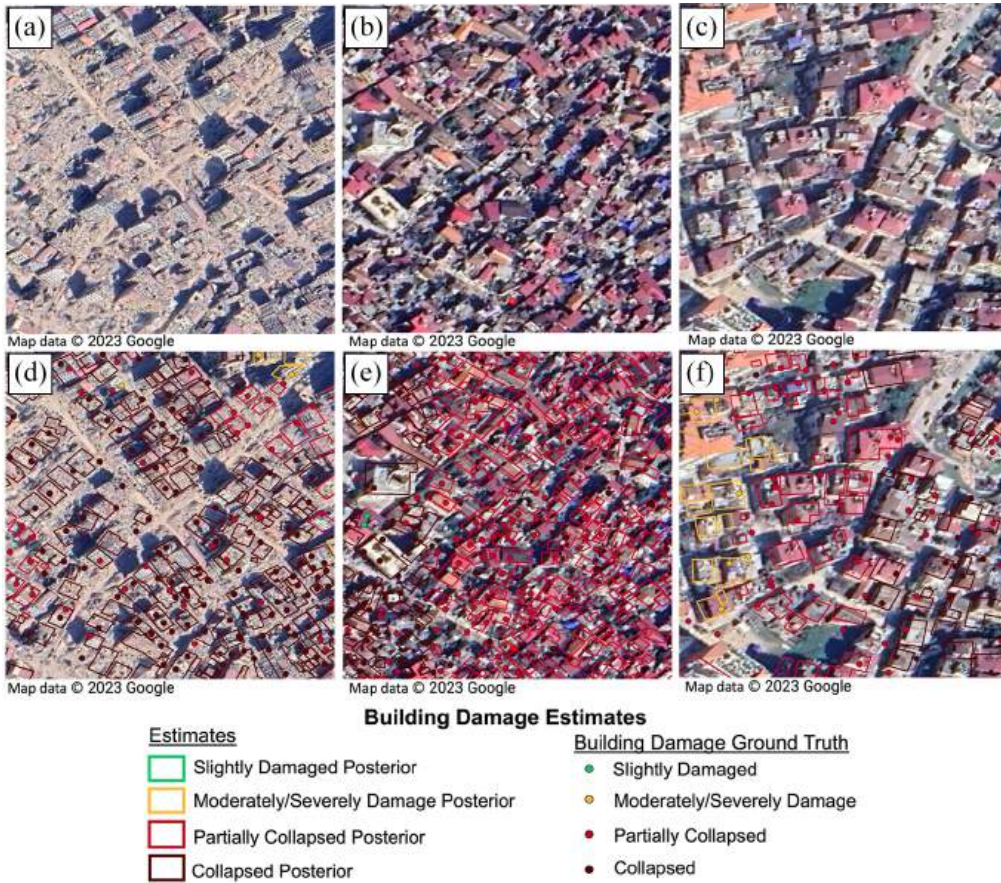


**Figure 9. Predicted building damage probability maps in Hatay.** Figures (a)–(c) show the satellite images, and Figures (d)–(f) present the corresponding building damage estimates with ground truth information. The legend colors represent the building damage levels, as indicated. The geographic extent of each figure is given in Table 4 and Figure 15(1).

indicates perfect separability between positive and negative classes. The study’s framework and benchmark methods output probability estimates of ground failure or building damage, which are then categorized as “no damage” or “damage” using a threshold. Since the threshold varies between events, the ROC curve visualizes how the system’s performance changes under varying thresholds ranging from 0 to 1. The ROC curves and AUC values for multi-categorical building damage models for the 2023 Turkey–Syria earthquake sequence are presented in Figure 11 and Table 3, respectively. The AUC results of our building damage models, which are all above 0.95, suggesting that the posterior models generated by our algorithm are able to make reasonably accurate estimates. Furthermore, in order to demonstrate the efficiency of our proposed framework with large-scale applications, we have assessed the computational efficiency of our model. Our variational inference framework can efficiently process estimates for the most moderately damaged areas (with covered areas of  $285 \text{ km}^2$ ,  $13,560 \text{ km}^2$ , and  $10,309 \text{ km}^2$ ), including Hatay, Osmaniye, Gaziantep, Kahramanmaraş, and Adiyaman, producing accurate results with computational times ranging from 2 to 200 minutes. This represents a significant improvement in





**Figure 10. Predicted building damage probability maps in İskenderun.** Figures (a)–(c) show the satellite images, and Figures (d)–(f) present the corresponding building damage estimates with ground truth information. The legend colors represent the building damage levels, as indicated. The geographic extent of each figure is given in Table 4 and Figure 15(2).

**Table 2.** Reported building damage levels percentages in regions studied. Reported data was obtained from ground-based reports.

Region	Slightly damaged count (%)	Moderately/severely damaged count (%)	Partially collapsed count (%)	Collapsed count (%)
Adiyaman	62.06	27.02	2.46	8.46
Gaziantep and Kahramanmaraş	70.95	20.30	3.10	5.65
Hatay and Osmaniye	56.33	30.51	4.21	8.95

efficiency, potentially reducing analysis time by hours or even days compared with most current methods, which generally do not offer the same level of resolution or detailed building-by-building assessments.

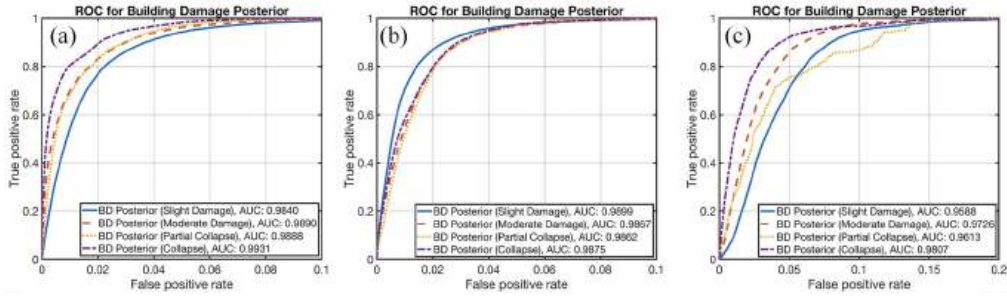


**Figure 11. ROC curves of the Turkey earthquake building damage posterior.** Figure (a) shows the ROC curve of the posterior in Hatay, Osmaniye, etc. area; (b) displays the ROC curve of the posterior in Kahramanmaraş and Gaziantep area; and (c) presents ROC curve of the posterior in Adiyaman area.

**Table 3.** The evaluation of our framework performance when predicting binary and multi-categorical building damage levels.

Cases	$AUC_{Post}$
Slightly damaged posterior in Figure 11(a)	0.9840
Moderately/severely damaged posterior in Figure 11(a)	0.9890
Partial collapsed posterior in Figure 11(a)	0.9888
Collapsed posterior in Figure 11(a)	0.9931
Slightly damaged in Figure 11(b)	0.9899
Moderately/severely damaged posterior in Figure 11(b)	0.9867
Partial collapsed posterior in Figure 11(b)	0.9862
Collapsed posterior in Figure 11(b)	0.9875
Slightly damaged posterior in Figure 11(c)	0.9588
Moderately/severely damaged posterior in Figure 11(c)	0.9726
Partial collapsed posterior in Figure 11(c)	0.9613
Collapsed posterior in Figure 11(c)	0.9807

Other than the AUC values, Figure 12 shows the confusion matrices for the assessment of our model's performance. The inclusion of confusion matrices alongside ROC curves for assessing a model's performance in classifying earthquake damage to buildings offers a detailed perspective on its capabilities, essential for real-world applications. The confusion matrices for the Hatay, Osmaniye, and other areas, Kahramanmaraş and Gaziantep area, and the Adiyaman area demonstrate the model's effectiveness in accurately identifying instances of slight damage and partial collapse. For example, in the Hatay and Osmaniye area, slight damage was correctly identified in 92.3% of cases, while partial collapse was accurately detected in 87.6% of instances. The model misclassified only 4.8% of slight damage cases as moderate damage. These high true positive rates and low misclassification percentages suggest the model's ability to distinguish these damage levels effectively.

Nevertheless, the matrices also uncover some confusion between adjacent severity classes. In the Kahramanmaraş and Gaziantep area, 18.2% of moderate damage cases were misclassified as slight damage. In Adiyaman, 12.5% of complete collapse cases were incorrectly classified as partial collapse, highlighting an area for model refinement, especially in differentiating the highest severity class.

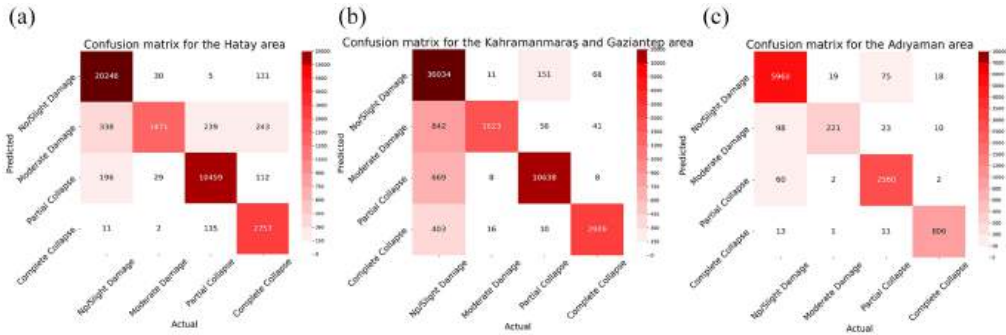


**Figure 12. Confusion matrices of the Turkey earthquake building damage posterior.** Figure (a) shows the confusion matrix of the posterior in Hatay, Osmaniye, etc. area; (b) displays the confusion matrix of the posterior in Kahramanmaraş and Gaziantep area; and (c) presents confusion matrix of the posterior in Adiyaman area.

**Table 4.** This table contains the extents of our building damage estimates visualization in Figures 5–8.

Figure	Extent
Figure 5(a)(d)	from 36.927 °E to 36.929 °E, from 37.568 °N to 37.575 °N (shown in Figure 13(1)(a))
Figure 5(b)(e)	from 36.921 °E to 36.929 °E, from 37.569 °N to 37.575 °N (shown in Figure 13(1)(b))
Figure 5(c)(f)	from 36.902 °E to 36.908 °E, from 37.588 °N to 37.594 °N (shown in Figure 13(1)(c))
Figure 6(a)(d)	from 36.252 °E to 36.266 °E, from 37.081 °N to 37.084 °N (shown in Figure 13(2)(a))
Figure 6(b)(e)	from 36.241 °E to 36.244 °E, from 37.069 °N to 37.273 °N (shown in Figure 13(2)(b))
Figure 6(c)(f)	from 36.240 °E to 36.243 °E, from 37.063 °N to 37.067 °N (shown in Figure 13(2)(c))
Figure 7(a)(d)	from 37.382 °E to 37.385 °E, from 37.068 °N to 37.072 °N (shown in Figure 14(1)(a))
Figure 7(b)(e)	from 37.371 °E to 37.373 °E, from 37.057 °N to 37.059 °N (shown in Figure 14(1)(b))
Figure 7(c)(f)	from 37.383 °E to 37.387 °E, from 37.081 °N to 37.084 °N (shown in Figure 14(1)(c))
Figure 8(a)(d)	from 38.258 °E to 38.262 °E, from 37.767 °N to 37.771 °N (shown in Figure 14(2)(a))
Figure 8(b)(e)	from 38.283 °E to 38.286 °E, from 37.760 °N to 37.763 °N (shown in Figure 14(2)(b))
Figure 8(c)(f)	from 38.272 °E to 28.275 °E, from 37.756 °N to 37.759 °N (shown in Figure 14(2)(c))
Figure 9(a)(d)	from 36.155 °E to 36.158 °E, from 36.205 °N to 36.208 °N (shown in Figure 15(1)(a))
Figure 9(b)(e)	from 36.167 °E to 36.169 °E, from 36.201 °N to 36.203 °N (shown in Figure 15(1)(b))
Figure 9(c)(f)	from 36.139 °E to 36.141 °E, from 36.207 °N to 36.209 °N (shown in Figure 15(1)(c))
Figure 10(a)(d)	from 36.147 °E to 36.154 °E, from 36.565 °N to 36.572 °N (shown in Figure 15(2)(a))
Figure 10(b)(e)	from 36.176 °E to 36.180 °E, from 36.575 °N to 36.579 °N (shown in Figure 15(2)(b))
Figure 10(c)(f)	from 36.193 °E to 36.197 °E, from 36.571 °N to 36.575 °N (shown in Figure 15(2)(c))

The comprehensive assessment provided by the high AUC values in the ROC curves, ranging from 0.9588 to 0.9931 across all regions and damage categories, corroborates the model’s overall robust predictive performance. Specifically, for the collapsed category, AUC values were 0.9931, 0.9875, and 0.9807 for Hatay/Osmaniye, Kahramanmaraş/Gaziantep, and Adiyaman areas respectively. This nuanced understanding is crucial for the model’s deployment in disaster response scenarios, where accurate damage classification directly impacts resource allocation and response strategies. The ROC curves were derived using a one-vs-all (OvA) approach for multi-class classification, which involves computing a separate binary classifier for each class against all others. This method allows for the detailed evaluation of each class’s ability to be distinguished from the rest, providing a clear overview of the model’s performance across different damage levels. By



**Figure 13.** Map illustrating the study areas within the region affected by ground shaking from the earthquake. Figure (1) shows the study area in Kahramanmaraş: (a) corresponds to Figure 5(a)(d), (b) corresponds to Figure 5(b)(e), and (c) corresponds to Figure 5(e)(f). Figure (2) shows the study area in Osmaniye: (a) corresponds to Figure 6(a)(d), (b) corresponds to Figure 6(b)(e), and (c) corresponds to Figure 6(e)(f).



**Figure 14.** Map illustrating the study areas within the region affected by ground shaking from the earthquake. Figure (1) shows the study area in Gaziantep: (a) corresponds to Figure 7(a) and (d), (b) corresponds to Figure 7(b) and (e), and (c) corresponds to Figure 7(e) and (f). Figure (2) shows the study area in Adıyaman: (a) corresponds to Figure 8(a) and (d), (b) corresponds to Figure 8(b) and (e), and (c) corresponds to Figure 8(e) and (f).

clarifying the evaluation process through this approach, we gain further insights into the model's classification capabilities, enabling a more informed assessment of its practical utility in earthquake-affected areas.

While our model demonstrates strong overall performance, it's important to note that this performance is not uniform across all regions studied. In particular, we observed some variations in model accuracy between different geographical areas. The analysis reveals a notable discrepancy in model performance across different regions, with the Kahramanmaraş and Gaziantep area showing relatively worse results compared with other regions. For instance, the AUC value for the collapsed category in Kahramanmaraş and Gaziantep (0.9875) is lower than that of Hatay/Osmaniye (0.9931), indicating a slightly reduced ability to accurately classify collapsed buildings in this area. Several factors may contribute to this regional variation in model performance: (1) The Kahramanmaraş and Gaziantep area may have more complex or varied geological conditions compared with other regions. This could lead to more nuanced ground motion patterns and subsequent building damage, which our model might find challenging to capture accurately. (2) The coverage and accuracy of building footprint data may vary between



**Figure 15.** Map illustrating the study areas within the region affected by ground shaking from the earthquake. Figure (1) shows the study area in Hatay: (a) corresponds to Figure 9(a) and (d), (b) corresponds to Figure 9(b) and (e), and (c) corresponds to Figure 9(c) and (f). Figure (2) shows the study area in Iskenderun: (a) corresponds to Figure 10(a) and (d), (b) corresponds to Figure 10(b) and (e), and (c) corresponds to Figure 10(c) and (f).

regions. Since we utilize building footprints in our pruning strategy to improve computational speed, the accuracy of building footprint data may influence the accuracy of our estimation results. If the Kahramanmaraş and Gaziantep area has less complete or less accurate building footprint data, this could significantly impact our model's ability to correctly identify and classify damaged buildings. Areas with more comprehensive building footprint data would likely yield better results. (3) There might be less comprehensive or less accurate ground truth data available for the Kahramanmaraş and Gaziantep region, affecting both model training and validation.

## Discussion

We employed our recently developed strategy to extract and portray building damage for the devastating Türkiye earthquake sequence and, for the first time, applied our tools in response mode, utilizing rapidly evolving models and data sources. Due to the availability of the dataset, our current methodology primarily estimates cumulative damage, employing the USGS' composite damage evaluation framework. The damage proxy maps are obtained by comparing the coherence change of pre-earthquake and post-earthquake SAR images, mainly capturing the accumulative/mixed surface ground changes between these periods. We utilized SAR images from Sentinel-1 collected on February 10, 2023, capturing the ground surface changes from September 19, 2022, to February 10, 2023, which includes both the devastating M 7.8 mainshock and M 7.5 aftershock.

Figure 16 presents a comprehensive matrix of fragility curves for building structures across three different geographical regions (Adiyaman area, Kahramanmaraş and Gaziantep area, and Hatay, Osmaniye, etc. area) and under three contrasting seismic conditions: severe landslides, severe liquefaction, and neither condition. Each panel within the matrix displays a fragility curve, marked by different levels of building damage—No/Slight Damage, Moderate Damage, Partial Collapse, and Complete Collapse—based on the peak ground acceleration (PGA) expressed as a percentage.

The graphs illustrate that buildings in areas with severe liquefaction or landslides exhibit a higher likelihood of damage at lower PGA levels, showcasing steeper slopes in these curves, which suggests a quicker escalation in damage as seismic intensity slightly increases. It is observed that the fragility curves for Kahramanmaraş and Gaziantep, as well as for

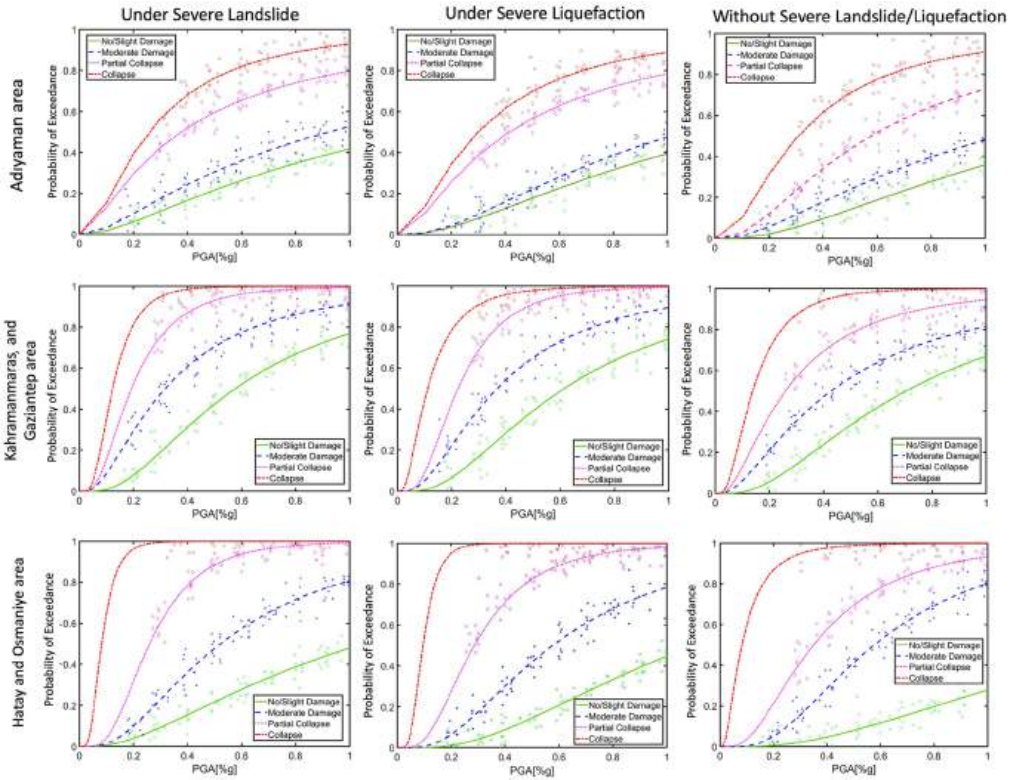


**Figure 16. Building damage probability estimation and fragility curve matrix for different locations and conditions.** This matrix illustrates the fragility curves derived from building damage probability estimations in three distinct regions, each subjected to various seismic conditions: severe landslide, severe liquefaction, and stable ground without severe landslide or liquefaction. The rows categorize the regions while the columns differentiate the conditions under which each fragility curve is drawn.

Hatay and Osmaniye, are steeper compared with those in Adiyaman. This implies that buildings in the former regions are more susceptible to damage at lower seismic intensities, likely due to factors such as local soil conditions, building practices, and previous seismic activities. The presence of severe liquefaction or landslides significantly exacerbates this vulnerability, resulting in a more pronounced damage probability even at lower intensities.

From the fragility curves, we can see that buildings are generally more likely to sustain moderate damage in areas with severe geological disturbances. This often corresponds to regions with high susceptibility to either landslides or liquefaction, which typically leads to a greater impact on the structural capacity of buildings. Furthermore, we only fit scenarios with severe landslides and severe liquefaction separately, not in combination, because landslides and liquefaction rarely occur simultaneously. Landslides usually result from slope failure induced by seismic activity, whereas liquefaction occurs in saturated soils under the stress of seismic waves. By analyzing these phenomena separately, we can more accurately gauge their distinct impacts on building integrity during earthquakes.

With the improvement of the revisiting frequency of SAR satellites, we expect to obtain more fine-grained temporal SAR images, like those from NASA-ISRO SAR (NISAR), which will help us better distinguish the causes in the time domain using the same technology. We acknowledge the importance of detailed time-series data in distinguishing the impacts of each seismic event more clearly. As satellite technology advances, allowing for more frequent revisits, we expect to obtain finer temporal resolution in SAR images, such as those from NISAR. This improvement will enhance our ability to analyze the temporal evolution of ground movements and correlate them with damage patterns, thereby improving the specificity and accuracy of our damage assessments. We showed that Damage proxy maps provide critical information at a regional scale yet provide building-specific damage. With these results, we are now more confident that we can generalize our method to other applications involving causal relations among compound ground failure and building damage caused by disasters, such as hurricanes and flooding.

We also quantified the causal relations between building damage and other disaster-induced ground failure. Ground shaking is always the most critical causal factor in the occurrence of building damage due to an earthquake (Xu et al. 2022b). However, we find that liquefaction and land subsidence at Golbasi, Turkey, also contributed substantially to building damage. Alternatively, in other events we studied earlier, such as the 2018 Hokkaido, Japan earthquake, and the 2016 Central Italy earthquake, notable contributions to building damage were due to landslides (Xu et al. 2022b), demonstrating that earthquake-induced building damage distribution patterns may differ significantly from event to event. Therefore, to accurately estimate hazards and their impacts, it is crucial to integrate prior knowledge of these hazards and quantify the causal relationships between different sources of building damage. This approach greatly benefits the estimation process by providing a more comprehensive understanding of the complex interactions among various hazards and their contributions to building damage.

It is important to note that our proposed method is capable of identifying the causes of damage even without prior knowledge from the field about which areas were subject to specific hazards such as liquefaction and landslides. However, incorporating prior knowledge, when available, can further enhance the accuracy and interpretability of the results by providing additional constraints and validating the inferred causal relationships. To quantify the contribution of prior knowledge to the model's predictive accuracy, we conduct an ablation study. This involves running the model with and without prior models of liquefaction and landslides. By comparing the model's performance in these two scenarios, we can assess the impact of prior knowledge on its ability to identify the causes of damage. It is worth noting that we only have ground truth data for building damage, and not for the specific hazards of liquefaction and landslides. Therefore, our ablation study focuses on evaluating the model's performance in estimating building damage under different input conditions, using the AUC as our accuracy metric.

As shown in Table 5, the full model achieves an AUC of 0.9840 for slightly damaged posterior, 0.9890 for moderately/severely damaged posterior, and 0.9888 for partial collapsed posterior in the Hatay, Osmaniye, etc. area. When we remove the prior models for landslides and liquefaction, the AUC values decrease to 0.8772, 0.8202, and 0.8104, respectively. This indicates that prior knowledge of these hazards contributes significantly to the model's predictive accuracy. Moreover, when we remove only the prior model for landslides or liquefaction, the AUC values fall between those of the full model and the model without any prior knowledge. This suggests that both landslides and liquefaction prior

**Table 5.** This table presents a comparison of the model's performance in Hatay, Osmaniye, etc. area across different configurations where specific input data related to prior model of liquefaction and landslides are systematically omitted.

Model variant	Cases	AUC
Full Model	Slightly damaged posterior	0.9840
	Moderately/severely damaged posterior	0.9890
	Partial collapsed posterior in Hatay, Osmaniye, etc. area	0.9888
	Collapsed posterior	0.9931
No Landslides Prior Model	Slightly damaged posterior	0.8772
	Moderately/severely damaged posterior	0.8202
	Partial collapsed posterior in Hatay, Osmaniye, etc. area	0.8104
	Collapsed posterior	0.7914
No Liquefaction Prior Model	Slightly damaged posterior	0.8717
	Moderately/severely damaged posterior	0.8510
	Partial collapsed posterior in Hatay, Osmaniye, etc. area	0.8475
	Collapsed posterior	0.8169
No Landslide and Liquefaction Prior Model	Slightly damaged posterior	0.7289
	Moderately/severely damaged posterior	0.7261
	Partial collapsed posterior in Hatay, Osmaniye, etc. area	0.7035
	Collapsed posterior	0.7242

models provide valuable information for estimating building damage, and their contributions are complementary.

Despite the absence of ground truth data for liquefaction and landslides, this ablation study provides valuable insights into the robustness and generalizability of our approach. It demonstrates the model's ability to leverage available information, even when direct measurements of certain hazards are lacking, to estimate the causes and extent of building damage. The results highlight the importance of incorporating prior knowledge when available, while also showcasing the model's capability to provide meaningful insights into the underlying factors contributing to damage, even in situations where prior field knowledge may be limited.

A key limitation of our method is the neglect of spatial influence from neighboring locations. For example, if a location is near a mountainous area with severe landslides, it will also tend to have severe landslides and building damage. However, our method assumes all locations in a map are independent without considering the influence of neighboring locations, which may result in inaccuracies.

Satellite imagery has become a valuable tool in identifying ground conditions in remote areas that are not easily accessible by disaster responders. With the improving timeliness and quality of such imagery, we recognized that tools are needed to fully exploit their potential for post-disaster situational awareness, response, and recovery. High-resolution images can also be generated by airborne SAR (Ekhtari and Glennie 2017), in a timely and efficient way. Our methodology can be combined with alternative high-resolution satellite images produced after a disaster to provide timely loss estimates. We have mapped out the natural evolution of our strategy that will further allow for random, timely ground failure and damage observations as further constraints in the form of immediate, event-specific training data.



Regarding the availability of publicly accessible high-quality satellite imagery for damage assessment in the 2023 Turkey–Syria earthquake, it can be considered typical compared with other recent earthquakes and natural disasters. For the 2023 Turkey–Syria earthquake, DPM were generated by the NASA Advanced Rapid Imaging and Analysis (ARIA) team using the Copernicus Sentinel-1 satellites operated by the European Space Agency (ESA) only four days post-event. This quick turnaround is representative of the capabilities and response times that have become increasingly common in the wake of significant natural disasters. Similarly, other earthquakes have benefitted from the availability of DPM generated by Sentinel-1, Japanese ALOS-2 satellite, NASA, NiSAR, and other commercial sources, illustrating a consistent trend towards rapid, accessible high-quality satellite imagery in disaster response scenarios.

In terms of ground failure models, the USGS routinely provides open-sourced ground failure models following significant earthquakes, which have been integral in assessing landslides and liquefaction risks. The USGS Ground Failure product offers near-real-time estimates of landslide and liquefaction hazards after significant earthquakes, highlighting the growing standard of these datasets for post-disaster analysis. Moreover, the widespread use of open-source platforms like OpenStreetMap has democratized the accessibility of detailed building footprints, which enhances the granularity of damage assessments. Combining these resources is a methodological approach that is becoming standardized in the field of disaster response and remote sensing.

Moreover, regarding the application of these methods to lower-resolution imagery (ranging from 5 meters to 30 meters), our previous work has explored this question in Xu et al. (2022b). The effectiveness of damage detection and assessment using lower-resolution imagery can vary but still provides valuable insights, especially when high-resolution imagery is not available. It is important to note that while high-resolution data typically yield more precise results, lower-resolution imagery can still be quite informative, especially when analyzed with robust models that can interpret broader patterns of damage.

## Conclusions

In this study, we predict building damage in the 2023 Turkey–Syria earthquake sequence by jointly estimating landslides, liquefaction, and building damage with consideration of their complex causal dependencies. We focus our approach on the simultaneous assessment of earthquake-induced building damage, landslides, and liquefaction without the need for ground truth data. Further, by leveraging building footprints, satellite imagery, and the shaking and ground failure models produced by the USGS as our prior hazard models, our approach achieves unprecedented damage resolution with unparalleled timeliness and regional scale, enabling well-informed decisions for reconnaissance, response, and recovery.

We validate our building damage probability maps by comparing them with optical satellite images from Google Maps taken on February 16, immediately after the earthquake sequence as well as against the building damage reports from Türkiye Ministry of Environment, Urbanization, last updated on 20 February 2023. Our results demonstrate the accuracy of our rapid building damage and multi-hazard estimation method. We released our building damage maps as early as ten days after the mainshock through ArcGIS online, and our initial results have been incorporated to assist front-line responding through Afet Platformu (<https://afetharitasi.org/>) and shared with reconnaissance teams via the DesignSafe (<https://www.designsafe-ci.org/>) data portal. According to our

assessment, Kahramanmaraş and Gaziantep have experienced moderate damage, whereas a majority of the buildings in Hatay, Osmaniye, and Adiyaman have undergone moderate damage or collapse. Buildings in the Kahramanmaraş area were mainly damaged by ground shaking but in Hatay and Adiyaman, liquefaction contributed considerably to building impacts. Our building damage model, with AUC results over 0.95, demonstrates that the posterior models created by our algorithm can produce accurate and highly useful building damage estimates. Furthermore, our method is capable of delivering post-disaster estimates for landslides and liquefaction. Initial comparisons indicate that our posterior landslide models supply a greater level of detail compared with the prior model, yet we await detailed survey observations now underway to fully assess their accuracy.

As currently deployed, we have been able to show that our method is able to produce accurate results rapidly, yet it is not by any means fully operational. We envision operationalizing our system to improve its timeliness, integrating ground-truth observations, and iterating as such reports evolve in order to update and refine our estimates further. Our study offers a promising approach for rapidly estimating building damage and ground failure after earthquakes using probabilistic models and causal relations. Such estimates can help with general situational awareness yet provide potentially much more accurate, actionable building-by-building damage inferences than earlier strategies. Lastly, the methodology we developed can be generalized to other types of disasters, such as hurricanes and flooding, to estimate the potential impacts and guide response and recovery measures.

### Acknowledgments

Any mention of commercial products is for informational purposes and does not constitute an endorsement by the U.S. government.


### Declaration of Conflicting Interests


The author(s) declared no potential conflicts of interest with respect to the research, authorship, and/or publication of this article.

### Funding

The author(s) disclosed receipt of the following financial support for the research, authorship, and/or publication of this article: X. L. and S. X. are supported by U.S. Geological Survey Grant G22AP00032 and NSF CMMI-2242590.

### ORCID iDs

Xuechun Li  <https://orcid.org/0009-0004-5067-4553>

David J. Wald  <https://orcid.org/0000-0002-1454-4514>

### Research Data and Code Availability

The underlying research materials related to this paper, including data, samples, and models, are accessible to interested researchers. Specifically:

**Data:** The datasets used in this study, including the high-resolution satellite imagery, ground failure models, and building footprint data, are available from publicly accessible sources. The damage proxy maps (DPM) used were generated by the NASA Advanced Rapid Imaging and Analysis (ARIA) team using the Copernicus Sentinel-1 satellites. These can be accessed through the ARIA Data Share platform <https://aria-share.jpl.nasa.gov/>. The USGS ShakeMap and ground failure

models are available through the US Geological Survey's Earthquake Hazards Program website <https://earthquake.usgs.gov/>. The building footprints can be obtained from OpenStreetMap at <https://www.openstreetmap.org/#map=4/38.01/-95.84>.

**Models:** The variational causal Bayesian network model and the algorithms used for building damage estimation are documented in the manuscript. The code is available at <https://github.com/SusuXu/VBCI>.

Researchers interested in accessing the data or models can contact the first author at X.L.

## References

- Allstadt KE, Thompson EM, Jibson RW, et al. (2022) The us geological survey ground failure product: Near-real-time estimates of earthquake-triggered landslides and liquefaction. *Earthquake Spectra* 38(1): 5–36.
- ARIA Data Share (2023a) Advanced rapid imaging and analysis (aria) – center for natural hazards. Online. URL [https://aria-share.jpl.nasa.gov/20230206\\_Turkey\\_EQ/DPM/](https://aria-share.jpl.nasa.gov/20230206_Turkey_EQ/DPM/).
- ARIA Data Share (2023b) Aria dpm sentinel-1 td21 v0.9, Türkiye and Syria. Online. URL [https://d1z62tir4fw0q0.cloudfront.net/20230206\\_Turkey\\_EQ/DPM/ARIA\\_DPM\\_Sentinel-1\\_Turkiye\\_EQ\\_caption.txt](https://d1z62tir4fw0q0.cloudfront.net/20230206_Turkey_EQ/DPM/ARIA_DPM_Sentinel-1_Turkiye_EQ_caption.txt).
- Bai Y, Hu J, Su J, et al. (2020) Pyramid pooling module-based semi-Siamese network: A benchmark model for assessing building damage from XBD satellite imagery datasets. *Remote Sensing* 12(24): 4055.
- Barras JA (2007) Satellite images and aerial photographs of the effects of hurricanes Katrina and Rita on coastal Louisiana. Technical report, U.S. Geological Survey.
- Bird JF, Bommer JJ, Crowley H, et al. (2006) Modelling liquefaction-induced building damage in earthquake loss estimation. *Soil Dynamics and Earthquake Engineering* 26(1): 15–30.
- Cetin KO, Soylemez B, Guzel H, et al. (2024) Soil liquefaction sites following the February 6, 2023, Kahramanmaraş-Türkiye earthquake sequence. *Bulletin of Earthquake Engineering* : 1–24.
- CrisisReady (2023) Magnitude 7.8 earthquake strikes Turkey and Syria, causes mass destruction and deaths. Online. URL <https://www.crisisready.io/2023/02/magnitude-7-8-earthquake-strikes-turkey-and-syria-causes-mass-destruction-and-deaths/>.
- Dilsiz A, Gunay S, Mosalam K, et al. (2023) Steer: 2023 mw 7.8 Kahramanmaras, Türkiye earthquake sequence preliminary virtual reconnaissance report (PVRR). DOI:10.17603/DS2-7RY2- GV66. URL <https://www.designsafe-ci.org/data/browser/public/designsafe.storage.published/PRJ-3824v2/#details-942732811040452115-242ac11b-0001-012>.
- Earle PS, Wald DJ, Jaiswal KS, et al. (2009) Prompt assessment of global earthquakes for response (pager): A system for rapidly determining the impact of earthquakes worldwide. *U.S. Geological Survey Open-File Report* : 15.
- Ekhtari N and Glennie C (2017) High-resolution mapping of near-field deformation with airborne earth observation data, a comparison study. *IEEE Transactions on Geoscience and Remote Sensing* 56(3): 1598–1614.
- Fan X, Scaringi G, Korup O, et al. (2019) Earthquake-induced chains of geologic hazards: Patterns, mechanisms, and impacts. *Reviews of Geophysics* 57(2): 421–503.
- Grünthal G (1998) *European Macroseismic Scale 1998 (EMS-98)*. Luxembourg: European Seismological Commission.
- Jaiswal K, Wald D and Porter K (2010) A global building inventory for earthquake loss estimation and risk management. *Earthquake Spectra* 26(3): 731–748.
- Lee S (2005) Application of logistic regression model and its validation for landslide susceptibility mapping using GIS and remote sensing data. *International Journal of Remote Sensing* 26(7): 1477–1491.
- Li X, Bürgi PM, Ma W, et al. (2023a) Disasternet: Causal Bayesian networks with normalizing flows for cascading hazards estimation from satellite imagery. In: *Proceedings of the 29th ACM SIGKDD Conference on Knowledge Discovery and Data Mining*. pp. 4391–4403.

- Li X, Dimasaka J, Zhang X, Yu X, et al. (2023b) M7.8 Turkey-Syria Earthquake Impact Estimates from Near-real-time Crowdsourced and Remote Sensing Data. *DesignSafe-CI*. DOI:10.17603/ds2-vns c-y870v2.
- Loos S, Lallemand D, Baker J, et al. (2020) G-dif: A geospatial data integration framework to rapidly estimate post-earthquake damage. *Earthquake Spectra* 36(4): 1695–1718.
- Maria T, Sotiris V, Efstratios K, et al. (2023) Preliminary mapping of liquefaction phenomena triggered by the February 6, 2023, m7.7 earthquake, Türkiye/Syria, based on remote sensing data. Technical report.
- Microsoft (2023) Global ml building footprints. Online. URL <https://github.com/microsoft/GlobalMLBuildingFootprints>.
- Nowicki JM, Hamburger M, Allstadt K, et al. (2018) A global empirical model for near-real-time assessment of seismically induced landslides. *Journal of Geophysical Research: Earth Surface* 123(8): 1835–1859.
- Ozkula G, Dowell RK, Baser T, et al. (2023) Field reconnaissance and observations from the February 6, 2023, Turkey earthquake sequence. *Natural Hazards* 119(1): 663–700.
- PreventionWeb (2023) Preliminary report on the February 6, 2023 earthquakes in Türkiye. Online. URL <https://www.preventionweb.net/news/preliminary-report-february-6-2023-earthquakes-turkiye>.
- SciTechDaily (2023) More than 100 landslides strike turkey following devastating earthquakes. Online. URL <https://scitechdaily.com/more-than-100-landslides-strike-turkey-following-devastating-earthquakes/>.
- Seismological Society of America (2023) Program for the 2023 turkey earthquake symposium. URL <https://meetings.seismosoc.org/wp-content/uploads/2023/04/SSA-Program-2023-Turkey-Earthquake-Rev-C.pdf>.
- US Geological Survey (2023a) M 7.5 - 4 km SSE of Ekinözü, turkey. Online. URL <https://earthquake.usgs.gov/earthquakes/eventpage/us6000jlqa/executive>.
- US Geological Survey (2023b) M 7.8 - 26 km ENE of Nurdağı, Turkey. Online. URL <https://earthquake.usgs.gov/earthquakes/eventpage/us6000jllz/executive>.
- US Geological Survey (2023c) M 7.8 - 26 km ENE of Nurdağı, Turkey - ground failure. Online. URL <https://earthquake.usgs.gov/earthquakes/eventpage/us6000jllz/ground-failure/summary>.
- US Geological Survey (2023d) M 7.8 - 26 km ENE of Nurdağı, Turkey - ShakeMap. Online. URL <https://earthquake.usgs.gov/earthquakes/eventpage/us6000jllz/shakemap/intensity>.
- US Geological Survey (2023e) M 7.8 - Pazarcik earthquake, Kahramanmaras earthquake sequence - ShakeMap. Online. URL <https://earthquake.usgs.gov/earthquakes/eventpage/us6000jllz/shakemap/intensity>.
- Wald D, Wald L, Worden B, et al. (2003) ShakeMap, a tool for earthquake response. Technical report.
- Wald DJ, Worden CB, Thompson EM, et al. (2022a) ShakeMap operations, policies, and procedures. *Earthquake Spectra* 38(1): 756–777.
- Wald DJ, Xu S, Noh H, et al. (2022b) Integrated strategies for enhanced rapid earthquake shaking, ground failure, and impact estimation employing remotely sensed and ground truth constraints. *Proceedings of the 12NCEE*.
- Wang C, Engler D, Li X, et al. (2023a) Near-real-time earthquake-induced fatality estimation using crowdsourced data and large-language models. *arXiv preprint arXiv:2312.03755*.
- Wang C, Liu Y, Zhang X, et al. (2023b) Causality-informed rapid post-hurricane building damage detection in large scale from InSAR imagery. In: *Proceedings of the 8th ACM SIGSPATIAL International Workshop on Security Response using GIS*, pp. 7–12.
- Worden C, Gerstenberger M, Rhoades D, et al. (2012) Probabilistic relationships between ground-motion parameters and modified Mercalli intensity in California. *Bulletin of the Seismological Society of America* 102(1): 204–221.
- Xu S, Dimasaka J, Wald DJ, et al. (2022a) Bayesian updating of seismic ground failure estimates via causal graphical models and satellite imagery. *The 17th World Conference on Earthquake Engineering*.

- Xu S, Dimasaka J, Wald DJ, et al. (2022b) Seismic multi-hazard and impact estimation via causal inference from satellite imagery. *Nature Communications* 13(1): 1–13.
- Xu S, Li X, Noh H, et al. (2022c) Deep causal Bayesian network for modeling spatial seismic building damage from remote sensing observations. In: *AGU Fall Meeting Abstracts*, volume 2022. pp. INV44A–02.
- Xu S and Noh HY (2021) Phymdan: Physics-informed knowledge transfer between buildings for seismic damage diagnosis through adversarial learning. *Mechanical Systems and Signal Processing* 151: 107374.
- Yu X, Hu X, Song Y, et al. (2024) Intelligent assessment of building damage of 2023 Turkey-Syria earthquake by multiple remote sensing approaches. *NPJ Natural Hazards* 1(1): 3.
- Yun SH, Fielding EJ, Webb FH, et al. (2015) Damage proxy map from interferometric synthetic aperture radar coherence. *US Patent* 9,207,318.
- Zhao C and Lu Z (2018) Remote sensing of landslides—a review. *Remote Sensing* 10(2): 279.
- Zhu J, Daley D, Baise LG, et al. (2015) A geospatial liquefaction model for rapid response and loss estimation. *Earthquake Spectra* 31(3): 1813–1837.